Available online at www.sciencedirect.com

ScienceDirect

IFAC PapersOnline CONFERENCE PAPER ARCHIVE

IFAC PapersOnLine 54-6 (2021) 359–364

Embedded Real-Time Nonlinear Model Predictive Control for the Thermal Torque Derating of an Electric Vehicle

Alexander Winkler * **Jonathan Frey** ** **Timm Fahrbach** *
Gianluca Frison ** **René Scheer** * **Moritz Diehl** **
Jakob Andert *

* *Teaching and Research Area for Mechatronics in Mobile Propulsion - RWTH Aachen University, Forckenbeckstraße 4, 52074 Aachen, Germany, (e-mail: {andert, winkler_a}@vka.rwth-aachen.de).*
** *Department of Microsystems Engineering, Albert-Ludwigs-University of Freiburg, Georges-Köhler-Allee 103, 79110 Freiburg, Germany, (e-mail: {jonathan.frey, diehl}@imtek.uni-freiburg.de).*

Abstract: This paper presents a real-time capable nonlinear model predictive control (NMPC) strategy to effectively control the driving performance of an electric vehicle (EV) while optimizing thermal utilization. The prediction model is based on an experimentally validated two-node lumped parameter thermal network (LPTN) and one-dimensional driving dynamics. An efficient solver for the trajectory tracking problem is exported using `acados` and deployed on a `dSPACE SCALEXIO` embedded system. The lap time of a high-load driving cycle compared to a state-of-the-art derating strategy improved by 2.56% with an energy consumption reduction of 2.43% while respecting the temperature constraints of the electric drive.

Keywords: nonlinear model predictive control, real-time control, automotive control, optimal control, permanent magnet motors, embedded systems, temperature control

1. INTRODUCTION

Permanent magnet synchronous machines (PMSM) have gained relevance in mobile propulsion due to their high torque and power density as well as efficiency. A consequence of the high power density is a highly locally concentrated heat generation. In conjunction with small installation space and the resulting limited cooling options, the machine is subject to intensive thermal loads during high and dynamic load operations such as overtaking maneuvers or race track runs. This creates the risk of irreversible demagnetization of the permanent magnets as well as damaging the foil insulation of the end windings causing short circuits. Those kind of failures would ultimately lead to a costly and time-consuming replacement of the electrical machine (EM). In order to avoid such measures and protect the machine components thermal derating is applied, directly reducing the requested torque of the machine as the temperatures approach critical values. Furthermore, thermal derating can save manufacturing costs by reducing the necessity for over-dimensioning the electrical machine, inverter and cooling system (Engelhardt, 2017). On the other hand, the temperature of the electrical machine has a major influence on its efficiency. Thus, thermal derating can provide higher thermal utilization by directly taking the economics of the electric drive into account.

In practice, thermal derating is usually implemented using simple rule-based control methods, such as a piecewise linear function or look-up-tables (LUT) that map a temperature to a derating factor. These control strategies reduce or shut down the output torque according to the current motor temperature (Engelhardt, 2017). This limits power significantly since linear derating strategies do not take the thermal dynamics of the electrical machine into account (Etzold et al., 2019). More recently, standard techniques such as proportional integral (PI) or linear–quadratic regulator (LQR) controllers have been implemented to reduce this gap by considering the thermal state of the electrical machine (Wallscheid and Böcker, 2017). Naturally, these control concepts cannot prevent temperature overshoots during high torque demands. This leads to conservative parametrization of these controllers, whereby output power is withheld. To prevent any violation of temperature constraints while exploiting the full thermal potential, future driving situations have to be taken into account (Wallscheid and Böcker, 2017).

Model predictive control (MPC) offers an explicit inclusion of constraints that are considered for the entire prediction horizon and is therefore well suited for this task as a predictive control (Grüne and Pannek, 2017). With the

⋆ The utilized hardware was provided by the Deutsche Forschungsgemeinschaft (German Research Foundation, DFG) – GRK 1856. Special thanks to DENSO AUTOMOTIVE Germany GmbH for providing the research electrical machine and the associated extensive thermal model and to the dSPACE GmbH for providing development support. This paper was written in the context of the Research Group (Forschungsgruppe) FOR 2401 “Optimization based Multi-scale Control for Low Temperature Combustion Engines”, which is funded by the Deutsche Forschungsgemeinschaft (German Research Foundation, DFG).

10.1016/j.ifacol.2021.08.570

principle of receding horizons an optimization problem is solved (approximately) at each sampling instance to determine the control input.

MPC in general has been frequently used for automotive control. A common approach is to use a linear MPC after linearizing the nonlinear process model once at a certain state to achieve real-time capability, see Griefnow et al. (2019). Kabzan et al. (2019) implemented an nonlinear model predictive control (NMPC) for autonomous racing in the context of Formula Student. Kloeser et al. (2020) achieved a real-time capable control of model cars while running the NMPC on a host computer. A different approach is hierarchical and multilevel MPC schemes for handling dynamic systems with different time scales, see Salazar et al. (2017).

NMPCs for thermal derating and thermal management in the automotive context have been utilized by several authors. Lopez Sanz et al. (2016) successfully implemented a slow dynamic thermal management model for a hybrid electric vehicle (HEV), validated by simulations. In Wallscheid and Böcker (2017), a direct torque control based on lumped parameter thermal network (LPTN) NMPC approach was proposed. Therein, a system model with more complex dynamics compared to the ones in this work was used. However, the authors did not look into real-time application on an embedded system.

To the best of our knowledge, the application of NMPC with highly dynamic models for thermal derating on embedded systems has not yet been satisfactorily investigated: the aim of the current contribution is to investigate this aspect and to develop a real-time capable NMPC in the automotive context. Thereto, this contribution incorporates the development and experimental validation of an NMPC based controller for the thermal derating of a battery electric vehicle (BEV). The proposed control strategy is presented and validated against state-of-the-art controllers, showing its real-time capability on an embedded platform. It is shown that thermal optimization by an NMPC can efficiently protect components from damage and improve the vehicle performance as well as the driving economics by exploiting the full thermal potential of the electrical machine.

The paper is organized as follows: Section 2 explains the utilized driving and thermal system model dynamics, while Section 3 presents the optimal control problem (OCP) formulation. In Section 4 the experimental setup regarding the utilized optimal control framework, solver and embedded system is shown. Section 5 presents and discusses the experimental results under consideration of the real-time capability. Finally, Section 6 concludes the paper with a summary and an outlook.

2. CONTROLLER MODELING

In this section, we derive model equations for the driving and thermal dynamics which will be used as prediction model for the MPC control in the subsequent section.

2.1 Driving Dynamics

The one-dimensional driving dynamics model consists of the longitudinal force equilibrium of the vehicle

Table 1. Electrical Machine (EM) and Vehicle Parameter

Parameter	Symbol	Value
EM peak power	$P_{\max}$	80 kW
EM peak torque	$T_{\max}$	160 Nm
EM peak revolutions	$n_{\max}$	14000 rpm
EM direct current (DC) link voltage	U_{DC}	300 V
Maximum EM temperature	$\vartheta_{\max}$	160 °C
Vehicle mass (incl. driver)	m_{veh}	1160 kg
Maximum vehicle speed	$v_{\max}$	130 km/h
Gear ratio	i	9.3
Cross section area	A_{c}	2.21 m^2
Drag coefficient	c_{d}	0.32
Rolling friction coefficient	c_{r}	0.011
Dynamic tyre radius	r_{dyn}	0.293 m

$$F_{\mathrm{Dem,W}} = F_{\mathrm{A}} + F_{\mathrm{S}} + F_{\mathrm{D}} + F_{\mathrm{R}}, \tag{1a}$$
$$F_{\mathrm{A}} = \dot{v} \cdot m_{\mathrm{veh}}, \tag{1b}$$
$$F_{\mathrm{S}} = m_{\mathrm{veh}} \cdot g \cdot \sin(\alpha_{\mathrm{s}}), \tag{1c}$$
$$F_{\mathrm{D}} = 0.5 \cdot c_{\mathrm{d}} \cdot A_{\mathrm{c}} \cdot \rho \cdot v^2, \tag{1d}$$
$$F_{\mathrm{R}} = m_{\mathrm{veh}} \cdot g \cdot \cos(\alpha_{\mathrm{s}}) \cdot c_{\mathrm{r}}, \tag{1e}$$

where F_{A}, F_{S}, F_{D}, F_{R} are the accelerating, slope, drag and rolling resistance forces, which together form the demand force on wheel level $F_{\mathrm{Dem,W}}$. Above, $\dot{v}$ is the derivative of the vehicle speed, m_{veh} the vehicle mass, g is the gravitational acceleration, α_{s} the road incline angle, c_{d} the drag coefficient, A_{c} the car's cross section area, ρ the air density and c_{r} the rolling friction coefficient. Rotational mass effects are neglected. The driving resistance force $F_{\mathrm{Dem,W}}$ is applied by the motor level drive force F_{M}. The latter can be transformed with the gear ratio i_{diff} and the dynamic wheel radius r_{dyn} to the motor level drive torque T_{M}, using

$$F_{\mathrm{Dem,W}} = F_{\mathrm{M}} \cdot i_{\mathrm{diff}} = T_{\mathrm{M}} \cdot i_{\mathrm{diff}} \cdot {r_{\mathrm{dyn}}}^{-1}. \tag{2}$$

For the temporal description of the vehicle movement, equations (1a) to (2) are reformulated to the ordinary differential equation (ODE) of the vehicle speed v:

$$\dot{v} = \frac{1}{m_{\mathrm{veh}}} \cdot (T_{\mathrm{M}} \cdot i_{\mathrm{diff}} \cdot {r_{\mathrm{dyn}}}^{-1} - m_{\mathrm{veh}} \cdot g \cdot \sin(\alpha_{\mathrm{s}}) - 0.5 \cdot c_{\mathrm{d}} \cdot A_{\mathrm{c}} \cdot \rho \cdot v^2 - m_{\mathrm{veh}} \cdot g \cdot \cos(\alpha_{\mathrm{s}}) \cdot c_{\mathrm{r}}). \tag{3}$$

As the controller has to differentiate between regenerative and friction braking, the motor level torque is divided to:

$$T_{\mathrm{M}} = T_{\mathrm{EM}} + T_{\mathrm{Fric,brk}} = T_{\mathrm{EM,acc}} + T_{\mathrm{EM,brk}} + T_{\mathrm{Fric,brk}}. \tag{4}$$

The friction brake torque $T_{\mathrm{Fric,brk}}$ and the electrical machine torque T_{EM} form the torque variables of the system on motor level. Furthermore, the EM torque is divided into the accelerating torque $T_{\mathrm{EM,acc}}$ and braking torque $T_{\mathrm{EM,brk}}$.

In this study, a typical mini car BEV is used with vehicle parameters as listed in Table 1. The data is validated using roll out tests of the vehicle as well as test bench measurements of the PMSM.

2.2 Thermal Machine Dynamics

In order to describe the thermal dynamics of the EM a two-node LPTN in accordance with Wallscheid and Böcker (2017) is used, see Figure 1.

Since only the two dominant heat paths are considered, the modeling depth and the computational complexity to

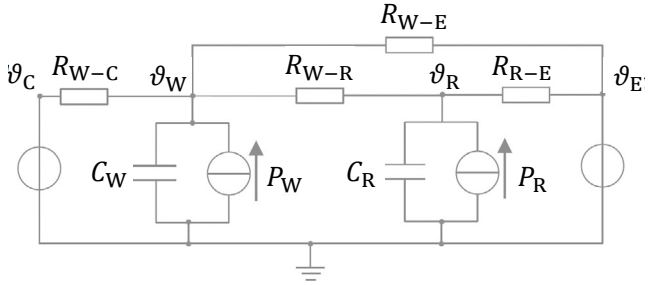

Fig. 1. Two-node lumped parameter thermal network (LPTN) to model machine temperatures.

evaluate the model are low. The LPTN consists of two temperature nodes for the winding temperature ϑ_{W} and the rotor temperature ϑ_{R} of the electrical machine. The quantities ϑ_{E} and ϑ_{C} describe the temperatures of the environment and the cooling liquid, which are assumed to be constant for simplicity of the model. The thermal behavior and the heat transfer between the nodes is described by the resistance $R_{\mathrm{i-j}}$ and capacitance C_{i} variables. The differential equations of the LPTN to calculate the change rate of the node temperatures are defined as

$$\dot{\vartheta_{\mathrm{R}}} = -\frac{1}{C_{\mathrm{R}}}\left(\frac{\vartheta_{\mathrm{R}} - \vartheta_{\mathrm{W}}}{R_{\mathrm{W-R}}} + \frac{\vartheta_{\mathrm{R}} - \vartheta_{\mathrm{E}}}{R_{\mathrm{R-E}}}\right) + \frac{P_{\mathrm{R}}}{C_{\mathrm{R}}}, \tag{5}$$

$$\dot{\vartheta_{\mathrm{W}}} = -\frac{1}{C_{\mathrm{W}}}\left(\frac{\vartheta_{\mathrm{W}} - \vartheta_{\mathrm{C}}}{R_{\mathrm{W-C}}} + \frac{\vartheta_{\mathrm{W}} - \vartheta_{\mathrm{E}}}{R_{\mathrm{W-E}}} + \frac{\vartheta_{\mathrm{W}} - \vartheta_{\mathrm{R}}}{R_{\mathrm{W-R}}}\right) + \frac{P_{\mathrm{W}}}{C_{\mathrm{W}}}. \tag{6}$$

The thermal network's heat sources are described by the winding power losses P_{W} and rotor power losses P_{R} of the PMSM as below

$$P_{\mathrm{R}} = 0.2 \cdot P_{\mathrm{L,Iron}} + \sigma\left(T_{\mathrm{EM}}\right) \cdot P_{\mathrm{L,Fric}}, \tag{7}$$

$$P_{\mathrm{W}} = P_{\mathrm{L,Ohm}} + 0.8 \cdot P_{\mathrm{L,Iron}}. \tag{8}$$

The iron losses $P_{\mathrm{L,Iron}}$ are distributed to the rotor and winding losses with constant parts of 0.2 and 0.8, respectively. This distribution was determined by explicit simulations of the PMSM manufacturer and is not directly applicable to other machines. The sign of the friction losses in equation (7) is dependent on the torque output of the machine. In order to ensure continuous differentiability, we use the sigmoid function $\sigma(\cdot) = \tanh(\frac{\cdot}{\varepsilon})$ with $\varepsilon = 10^{-3}$. A particle swarm optimization (PSO) is used to parametrize the LPTN variables with test bench stimulation curves. The aforementioned losses are calculated according to

$$P_{\mathrm{L,Ohm}} = 3 \cdot {i_{\mathrm{ph}}}^2 \cdot R_{\mathrm{W},0} \cdot \left(1 + \alpha_{\mathrm{Co}} \cdot \left(\vartheta_{\mathrm{W}} - \vartheta_{\mathrm{W},0}\right)\right), \tag{9}$$

$$P_{\mathrm{L,Fric}} = 2\pi \cdot n_{\mathrm{EM}} \cdot T_{\mathrm{Fric}}, \tag{10}$$

$$P_{\mathrm{L,Iron}} = P_{\mathrm{El,AC}} - P_{\mathrm{Mech}} - P_{\mathrm{L,Ohm}} - P_{\mathrm{L,Fric}}, \tag{11}$$

$$\text{with} \quad n_{\mathrm{EM}} = \frac{30 \cdot v \cdot i_{\mathrm{diff}}}{\pi \cdot r_{\mathrm{dyn}}}.$$

To consider the temperature dependency of the phase current i_{ph} and the phase resistance R_{ph}, the latter is calculated with the measured winding resistance at reference temperature $R_{\mathrm{W},0}$, the temperature coefficient of copper α_{Co} and the windings' temperature difference to the reference temperature. T_{Fric} is determined by test bench measurements of the machine. The iron losses are quantified indirectly by calculating the difference to the machines total losses, including the alternating current power $P_{\mathrm{El,AC}}$ and mechanical output power P_{Mech}.

For a computationally efficient and numerically suitable use in the NMPC, the power loss maps $P_{\mathrm{L,Ohm}}, P_{\mathrm{L,Fric}}$, $P_{\mathrm{L,Iron}}$ are approximated by third degree polynomials:

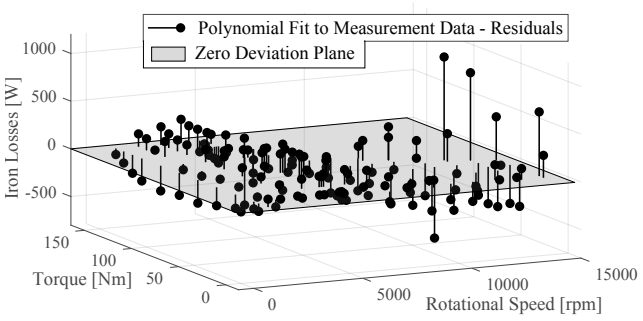

Fig. 2. Residuals of polynomial regression on iron losses of test bench measurements of the electrical machine.

$$P_{\mathrm{L},*} \approx \sum_{i=0}^{3} \sum_{j=0}^{3-i} p_{ij}^{*} \cdot {T_{\mathrm{EM}}}^{i} \cdot {n_{\mathrm{EM}}}^{j}, \tag{12}$$

for $* \in \{\mathrm{Ohm}, \mathrm{Fric}, \mathrm{Iron}\}$ where the coefficients p_{ij}^{*} have been determined by regressions. Figure 2 shows the absolute residuals of one of the aforementioned polynomial regression to the iron losses of the utilized electrical machine. The iron losses were calculated from test bench measurements according to equation (11). The displayed regression has an R-squared value of 96% and a root-mean-square-error (RMSE) of 236.85 W. All of the approximations performed have an R-squared value to the test bench data between 90% and 96% and were therefore considered to be sufficiently accurate.

3. PROBLEM FORMULATION & SOLUTION

The prediction model for the MPC will comprise the states of the one-dimensional vehicle model v and ϑ_{R}, ϑ_{W} from the LPTN model. Moreover, we formulate the actuators of the system as states and their time derivatives as control inputs, in order to limit oscillations of the actuators via constraints within a nonlinear program (NLP) with OCP sparsity structure. Thus, the prediction model consists of the state vector x, the control vector u and the parameter p, which are defined as

$$\begin{aligned} x &= \left[\vartheta_{\mathrm{R}}, \vartheta_{\mathrm{W}}, v, T_{\mathrm{EM,acc}}, T_{\mathrm{EM,brk}}, T_{\mathrm{Fric,brk}}\right]^{T}, \\ u &= \left[u_{\mathrm{EM,acc}}, u_{\mathrm{EM,brk}}, u_{\mathrm{Fric,brk}}\right]^{T}, \\ p &= \alpha_{\mathrm{s}}. \end{aligned} \tag{13}$$

The road slope angle α_{s} is stated as an external parameter of the system. The dynamics of the states $T_{\mathrm{EM,acc}}, T_{\mathrm{EM,brk}}, T_{\mathrm{Fric,brk}}$ are trivially given by

$$\begin{aligned} \dot{T}_{\mathrm{EM,acc}} &= u_{\mathrm{EM,acc}}, \\ \dot{T}_{\mathrm{EM,brk}} &= u_{\mathrm{EM,brk}}, \\ \dot{T}_{\mathrm{Fric,brk}} &= u_{\mathrm{Fric,brk}}. \end{aligned} \tag{14}$$

Consequently, the ODE describing the behavior of (13) is given by equations (3), (5), (6), (14) and summarized as

$$\begin{aligned} \dot{x} &= f(x(t), u(t), p) \\ &= \left[\dot{\vartheta}_{\mathrm{R}}, \dot{\vartheta}_{\mathrm{W}}, \dot{v}, \dot{T}_{\mathrm{EM,acc}}, \dot{T}_{\mathrm{EM,brk}}, \dot{T}_{\mathrm{Fric,brk}}\right]^{T}. \end{aligned} \tag{15}$$

This nonlinear ODE is discretized using 4 steps of the explicit Runge-Kutta method of order 4 over a time interval of 0.1s. The discrete-time dynamic system is denoted as

$$x_{k+1} = \phi(x_k, u_k). \tag{16}$$

We use the multiple shooting parametrization scheme to directly formulate a discrete OCP structured NLP with N shooting nodes, the discrete-time dynamic system in (16), a state trajectory $\boldsymbol{x} = [x_0, \dots, x_N]$ and a control trajectory $\boldsymbol{u} = [u_0, \dots, u_{N-1}]$.

We define the nonlinear inequality constraint function $g(\cdot)$ to describe the output power of the electrical machine $P_{\mathrm{EM,max}}$ and the equality constraint function $h(\cdot)$ to prevent of simultaneous accelerating and braking as follows:

$$g(x,u) = P_{\mathrm{EM}} - P_{\mathrm{EM,max}} = |T_{\mathrm{EM}}| \cdot \frac{v \cdot i_{\mathrm{diff}}}{r_{\mathrm{dyn}}} - P_{\mathrm{EM,max}}, \quad (17)$$

$$h(u) = \begin{bmatrix} T_{\mathrm{EM,acc}} \cdot T_{\mathrm{EM,brk}} \\ T_{\mathrm{EM,acc}} \cdot T_{\mathrm{Fric,brk}} \end{bmatrix}. \quad (18)$$

The cost function $J(\boldsymbol{x},\boldsymbol{u})$ of the OCP is defined as

$$J(\boldsymbol{x},\boldsymbol{u}) = \sum_{k=0}^{N-1} \|y(x_k,u_k) - y_k\|_Q + \|y_{\mathrm{e}}(x_N) - y_N\|_{Q_{\mathrm{e}}} \quad (19a)$$

with

$$y(x,u) = [v, T_{\mathrm{EM,acc}}, T_{\mathrm{EM,brk}}, T_{\mathrm{Fric,brk}}, u_{\mathrm{EM,acc}}]^T, \quad (19b)$$

$$y_{\mathrm{e}}(x_N) = [v, T_{\mathrm{EM,acc}}, T_{\mathrm{EM,brk}}, T_{\mathrm{Fric,brk}}]^T, \quad (19c)$$

$$y_k = [v_{k,\mathrm{ref}}, 0, 0, 0, 0]^T, \quad (19d)$$

$$y_N = [v_{N,\mathrm{ref}}, 0, 0, 0, 0]^T, \quad (19e)$$

where (19b) and (19c) define the outputs whose deviation from the reference values is penalized in the Lagrange and Mayer term respectively. The quantities $v_{k,\mathrm{ref}}$ for $k = 0, \dots, N$ are the external reference vehicle speeds at shooting node k. This reference trajectory of the vehicle speed is generated offline externally, see Section 4 and Figure 3. The matrices Q and Q_{e} are the positive definite weight matrices of the Lagrange and Mayer term, respectively, and have been varied in the experiments as mentioned in Section 5.

We use the multiple shooting scheme to directly formulate a discrete OCP structured NLP:

$$\min_{\boldsymbol{x},\,\boldsymbol{u}} \quad J(\boldsymbol{x},\boldsymbol{u}) \quad (20a)$$

$$\text{s.t.} \quad x_0 = \bar{x}_0, \quad (20b)$$

$$x_{k+1} = \phi(x_k, u_k), \quad k = 0, \dots, N-1, \quad (20c)$$

$$\underline{x} \le x_k \le \overline{x}, \quad k = 0, \dots, N, \quad (20d)$$

$$\underline{u} \le u_k \le \overline{u}, \quad k = 0, \dots, N-1, \quad (20e)$$

$$0 \ge g_k(x_k, u_k), \quad k = 0, \dots, N, \quad (20f)$$

$$0 \ge g_N(x_N), \quad (20g)$$

$$0 = h_k(u_k), \quad k = 0, \dots, N-1. \quad (20h)$$

The problem can therefore be denoted as a trajectory tracking problem. The constraints (20f), (20g), (20h) are softened using slack variables, which are penalized with a linear-quadratic cost term to robustify the controller. In Table 2 the lower and upper values of the state and control constraints are listed.

4. EXPERIMENTAL SETUP

The NMPC and the control path model are developed in `MATLAB/Simulink`. Figure 3 shows the utilized control loop structure.

A highly accurate 70-node LPTN provided by the PMSM's manufacturer to model the thermal motor dynamics is included in the control path. It has the feature of reinitializing the coefficients and parameters at each time step. The driving dynamics of the control path are calculated with the identical one-dimensional model in (3). The control path model runs with an update rate of 100 Hz. As indicated in equation (19d) the vehicle speed is given an external trajectory as a reference value, simulated beforehand with the virtual test drive platform `IPG CarMaker`. The reference trajectory is updated in the control path depending on the car's actual track position.

Table 2. Constraint Values

Min Value $(\underline{x}, \underline{u})$	Variable (x, u)	Max Value $(\overline{x}, \overline{u})$
0 °C	$\vartheta_{\mathrm{W}}, \vartheta_{\mathrm{R}}$	155 °C
0 m/s	v	36.11 m/s
0 Nm	$T_{\mathrm{EM,acc}}$	160 Nm
160 Nm	$T_{\mathrm{EM,brk}}$	0 Nm
515 Nm	$T_{\mathrm{Fric,brk}}$	0 Nm
500 Nm/s	$u_{\mathrm{EM,acc}}$, $u_{\mathrm{EM,brk}}$, $u_{\mathrm{Fric,brk}}$	500 Nm/s

The real-time capability is verified using the `dSPACE SCALEXIO` Hardware-in-Loop (HiL) real-time system. The system is equipped with a 3.8 GHz processor quad core `Intel Xeon` and one of its cores is used to compute the NMPC feedback.

The chosen driving cycle is the Nürburgring Nordschleife race track. With its 20.8 km total length, 320 meters of difference in altitude and up to 17% incline, the track poses major challenges for the powertrain.

Depending on the car's track position, the reference trajectory is updated via longitudinal driving dynamics equations (1a) in the model-based environment for each simulation time step. This includes the road incline angle, which is passed to the controller as a parameter.

The NMPC is implemented using the optimal control software framework `acados` and its `MATLAB` and `Simulink` interface (Verschueren et al., 2020). A sequential quadratic programming (SQP) method with a real-time iteration (RTI) scheme is used to approximately solve the NLP in (20) (Diehl et al., 2002). Partial condensing as implemented in `HPIPM` is used to condense the OCP structured quadratic programs (QP) with horizon $N = 40$ into ones with horizon $\tilde{N} = 5$. The high-performance interior-point-method QP solver `HPIPM` based on the linear algebra package `BLASFEO` is used to solve the resulting OCP structured QPs (Frison and Diehl, 2020; Frison et al., 2020).

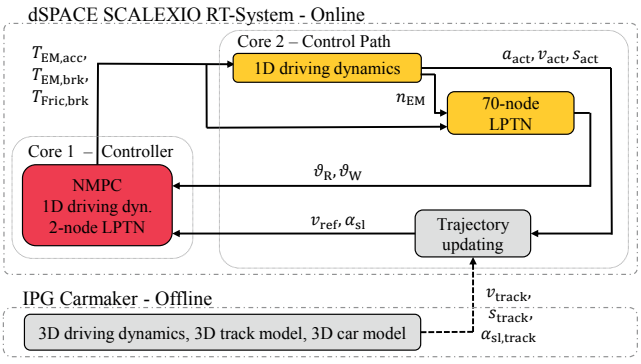

Fig. 3. Control loop structure and setup.

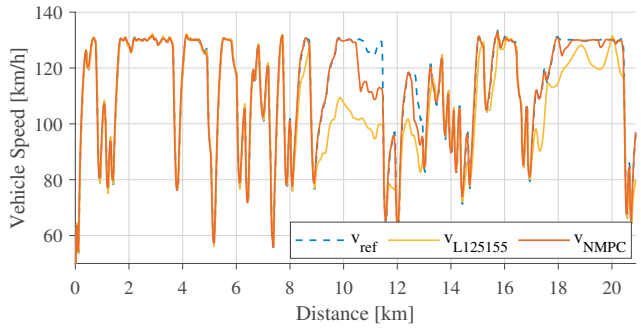

Fig. 4. Vehicle speed v of the NMPC in comparison to linear derating in one driving cycle.

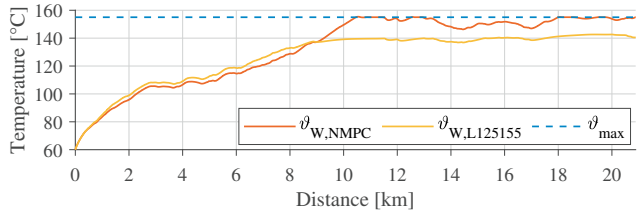

Fig. 5. Winding temperature ϑ_{W} of the NMPC in comparison to linear derating in one driving cycle.

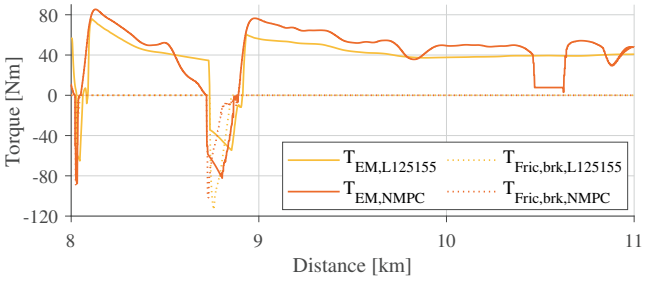

Fig. 6. Output torques of the NMPC in comparison to linear derating from km 8 to 11 of driving cycle.

The `acados` libraries have been cross-compiled for the `dSPACE SCALEXIO`. This was a major practical challenge of this work, as the `dSPACE` or `Simulink RTI` toolchain cannot be used to compile large custom libraries. The documentation of the workflow and the required toolchain files are about to be integrated in the `acados` repository.

5. RESULTS

The optimization-based NMPC control strategy is evaluated in terms of a comparison with the aforementioned linear derating approach. In Etzold et al. (2019) an optimal linear derating strategy was identified for the specific PMSM with HiL test bench experiments for the identical use-case. The so-called L125155 strategy operates with a derating start and end temperature of 125 °C and 155 °C respectively. Thus, the derating factor decreases linearly between $f_{\mathrm{Derating}}(\vartheta_{\mathrm{W}} = 125\ ^{\circ}\mathrm{C}) = 1$ and $f_{\mathrm{Derating}}(\vartheta_{\mathrm{W}} = 155\ ^{\circ}\mathrm{C}) = 0$. In a first step, the vehicle state results are investigated on one lap on the Nürburgring Nordschleife driving cycle of both the linear derating controlled vehicle and the NMPC controlled vehicle. All results are generated with the same setup to ensure comparability. The prediction horizon is divided into 40 intervals of length 0.1 s each.

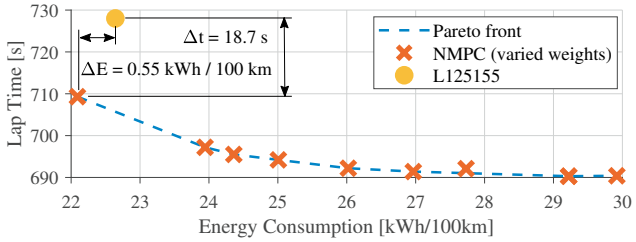

Fig. 7. Lap time and energy consumption results for NMPC with varied output torque weights.

In Figure 4 the vehicle speed obtained by the two control strategies and reference trajectory are visualized for one lap. One can easily observe that the NMPC controlled vehicle follows the reference trajectory more closely. Figure 5 shows the EM winding temperature ϑ_{W} for the lap of both control strategies as well as the temperature constraint of $\vartheta_{\max} = 155$ °C. The rotor temperature ϑ_{R} is not shown since it is not reaching critical temperatures with $\vartheta_{\mathrm{R}} \leq 110$ °C. Although the rotor temperature has an influence on the performance of the machine, this dependency is not represented in both the NMPC and the control path model and is therefore neglected in the analysis. Before reaching critical temperatures, the NMPC reduces the peak speeds, therefore reducing the thermal loads. In the region of high accelerations from a distance of 8 km on, the NMPC is able to deliver higher torques and thus reach higher vehicle speeds. This can be observed in Figure 6, where the output torques of the two control strategies are shown for an interesting part of the experiment. The linear derating approach significantly decreases the accelerating torque with respect to the reference after km 8 to conservatively not exceed the temperature constraints, as seen in Figure 5. Between km 10 and km 11 the torque of the EM is reduced by the NMPC to cope with an active temperature constraint. Thermal utilization is improved by the NMPC with increased output power while maintaining thermal boundary conditions. The predictive nature of the NMPC allows machine temperatures to be maintained at higher levels, thus achieving improved driving performance.

Moreover, the results are focused on the car's performance (indicated by the lap time) and the driving economics of the control strategy (indicated by the distance-related energy consumption in one lap). Figure 7 shows the lap time and energy consumption results of the linear derating L125155 and the NMPC controlled car. The weights of the actuator output torques in Q and Q_{e} of the NMPC are varied to change the controllers behavior regarding regenerative braking. When decreasing the cost weight corresponding to $T_{\mathrm{EM,brk}}$ regenerative braking is increased, thus the EM is heating up more and the lap time increases. Consequently, when increasing the weights on regenerative braking, the energy consumption is decreased, but the lap time and thus the car's performance are improved. An expected trade-off behavior between the car's energy consumption and track performance is shown. This parameter study of varying the cost function weights leads to the discrete Pareto front displayed in Figure 7. One can easily verify, that this Pareto front only consists of points that correspond to variants of the proposed NMPC controller. The NMPC improves the lap time by 18.7 s or 2.56% compared to the linear derating approach L125155

while reducing the energy consumption by 0.55 kWh / 100 km or 2.43%.

These results need to be reflected critically since both the NMPC and the control path model use an one-dimensional driving model, thus not taking lateral driving dynamics into account. The NMPC is able to partly reduce the braking torque in high-deceleration parts of the track to maintain lower machine temperatures, since the driving stability is not considered.

The computation time of the embedded controller never exceeds 23 ms while achieving a mean value of 6.45 ms. Therefore we achieve a more than 4-fold real-time capability on the embedded system with the proposed NMPC.

6. CONCLUSION

In this paper an embedded and real-time capable NMPC thermal torque derating strategy for an electric vehicle is presented. We showed that the NMPC is able to optimize the thermal utilization of the PMSM while respecting the temperature constraints. Thereto, a two-node LPTN of the machine thermal dynamics and one-dimensional driving dynamics model were parametrized and validated with test bench measurements. The OCP structured NLP was formulated using the high-performance optimization software package `acados` and embedded on the `dSPACE SCALEXIO` HiL real-time system to investigate real-time capability. In order to achieve low computation times, the real-time iteration (RTI) scheme combined with the efficient solver `HPIPM` was used. High-load race track simulations were conducted and the driving as well as the economic performance of the NMPC were analyzed in comparison to a state-of-the-art linear derating strategy. The NMPC was able to improve the lap time by 2.56% while decreasing the energy consumption by 2.43%. Moreover, we obtained an 4-fold real-time capability on the embedded system. This paper highlights the vast capability of NMPC and the utilized `acados` software package for embedded optimization based control in the automotive context of control engineering practice.

In this research, much of the focus was on real-time capability of the embedded optimization-based controller, thus using a relatively simple but computational efficient model. Since the proposed controller satisfies the real-time requirements with such a large margin, it looks promising that a similar NMPC strategy with a more complex model including lateral driving dynamics or a thermal model with variable coolant temperature can be implemented in a real-time feasible fashion. The additional computational complexity could be mitigated by using a structure-exploiting integrator (Frey et al., 2019). Further future work on this research topic will focus on the analysis of disturbances on the state variables and eventually full HiL test bench measurements involving the real electrical machine.

REFERENCES

Diehl, M., Bock, H., Schlöder, J.P., Findeisen, R., Nagy, Z., and Allgöwer, F. (2002). Real-time optimization and nonlinear model predictive control of processes governed by differential-algebraic equations. *Journal of Process Control*, 12(4), 577–585.

Engelhardt, T. (2017). *Derating-Strategien für elektrisch angetriebene Sportwagen*. Springer Fachmedien Wiesbaden, Wiesbaden.

Etzold, K., Fahrbach, T., Klein, S., Scheer, R., Guse, D., Klawitter, M., Pischinger, S., and Andert, J. (2019). Function development with an electric-machine-in-the-loop setup: A case study. *IEEE Transactions on Transportation Electrification*.

Frey, J., Quirynen, R., Kouzoupis, D., Frison, G., Geisler, J., Schild, A., and Diehl, M. (2019). Detecting and exploiting Generalized Nonlinear Static Feedback structures in DAE systems for MPC. In *Proceedings of the European Control Conference (ECC)*.

Frison, G. and Diehl, M. (2020). HPIPM: a high-performance quadratic programming framework for model predictive control. In *Proceedings of the IFAC World Congress*. Berlin, Germany.

Frison, G., Sartor, T., Zanelli, A., and Diehl, M. (2020). The BLAS API of BLASFEO: Optimizing performance for small matrices. *ACM Transactions on Mathematical Software (TOMS)*, 46(2), 15:1–15:36.

Griefnow, P., Andert, J., Xia, F., Klein, S., Stoffel, P., Engels, M., and Jolovic, D. (2019). Real-Time Modeling of a 48V P0 Mild Hybrid Vehicle with Electric Compressor for Model Predictive Control. In *SAE Technical Paper Series*. SAE International.

Grüne, L. and Pannek, J. (2017). *Nonlinear Model Predictive Control*. Springer International Publishing, Cham.

Kabzan, J., de la Iglesia Valls, M., Reijgwart, V., Hendrikx, H.F.C., Ehmke, C., Prajapat, M., Bühler, A., Gosala, N.B., Gupta, M., Sivanesan, R., Dhall, A., Chisari, E., Karnchanachari, N., Brits, S., Dangel, M., Sa, I., Dubé, R., Gawel, A., Pfeiffer, M., Liniger, A., Lygeros, J., and Siegwart, R. (2019). AMZ driverless: The full autonomous racing system. *CoRR*, abs/1905.05150.

Kloeser, D., Schoels, T., Sartor, T., Zanelli, A., Frison, G., and Diehl, M. (2020). NMPC for racing using a singularity-free path-parametric model with obstacle avoidance. In *Proceedings of the IFAC World Congress*.

Lopez Sanz, J., Ocampo-Martinez, C., Alvarez-Florez, J., Moreno Eguilaz, M., Ruiz-Mansilla, R., Kalmus, J., Graber, M., and Lux, G. (2016). Nonlinear model predictive control for thermal management in plug-in hybrid electric vehicles. *IEEE Transactions on Vehicular Technology*.

Salazar, M., Balerna, C., Elbert, P., Grando, F.P., and Onder, C.H. (2017). Real-time control algorithms for a hybrid electric race car using a two-level model predictive control scheme. *IEEE Transactions on Vehicular Technology*, 66(12), 10911–10922.

Verschueren, R., Frison, G., Kouzoupis, D., Frey, J., van Duijkeren, N., Zanelli, A., Novoselnik, B., Albin, T., Quirynen, R., and Diehl, M. (2020). acados: a modular open-source framework for fast embedded optimal control.

Wallscheid, O. and Böcker, J. (eds.) (2017). *Derating of Automotive Drive Systems Using Model Predictive Control*. IEEE, Piscataway, NJ.